Materials Letters 396 (2025) 138742

Contents lists available at ScienceDirect

Materials Letters

journal homepage: www.elsevier.com/locate/matlet

Synchrotron investigation of heat treatment effects on the 3D residual stress distribution in laser powder bed fused AlSi7Mg alloys

A. Rahimi [a], M. Coduri [b,c,*], A. Fitch [d], M. Vedani [a], J. Schröder [e], G. Bruno [e], R. Casati [a,*]

[a] Dept. of Mechanical Engineering, Politecnico di Milano 20156 Milano, Italy
[b] Dept. of Chemistry, University of Pavia 27100 Pavia, Italy
[c] INSTM, 50121 Florence, Italy
[d] ESRF, European Synchrotron Radiation Facility, 38000 Grenoble, France
[e] BAM, Bundesanstalt für Materialforschung und -prüfung, 12205 Berlin, Germany

ARTICLE INFO

Keywords:
Residual stresses
Laser powder bed fusion
Synchrotron diffraction
Heat treatment

ABSTRACT

For the first time, we utilized synchrotron diffraction to determine 3D maps of residual stresses across the entire volume of thick AlSi7Mg alloy prisms produced by PBF-LB. Samples were subjected to different heat treatment processes: direct aging (T5), solution treatment, and solution treatment followed by aging (T6). The T6 heat treatment resulted in the lowest residual tensile strains, while the T5 treatment resulted in significantly higher residual strains. Maximum residual stresses decreased from the as-built condition to the T6 heat-treated specimen. Although the T5 condition provides greater strength, it also retains higher tensile residual stresses near the surface, which can negatively affect fatigue properties.

1. Introduction

Age-hardenable AlSi7Mg alloy is commonly used in Laser Powder Bed Fusion (PBF-LB), thanks to its low susceptibility to hot-cracking, high corrosion resistance and good mechanical performance [1]. Direct aging from as-built condition (DA, T5 temper) and conventional solution treatment followed by aging (STA, T6 temper) lead to significantly different mechanical properties [2–4]. The static mechanical properties of the AlSi7Mg alloy produced by PBF-LB are summarized in Table S1, in the Supplementary Material. The highest tensile strength is achieved by applying a T5 temper. However, the same treatment leads to the lowest fracture toughness value in samples with cracks aligned with boundaries between layers. By the T6 temper, the strong anisotropic behaviour of the material can be overcome, at the cost of reduced strength and fracture toughness. Heat-treatment routes are also responsible for a drastic change in the stress state of the as-built material [3]. Residual stresses can lead to the part distortion, loss of geometric tolerance, cracking, and deterioration of fatigue performance and fracture resistance of printed parts [5].

Here, for the first time, we employed synchrotron radiation diffraction to determine 3D maps of the residual stresses throughout the full volume of thick AlSi7Mg alloy prisms fabricated by PBF-LB and subjected to various heat treatment schedules. This investigation offers valuable insights into optimizing heat treatment processes to improve the mechanical properties of PBF-LB Al parts, enabling their use in broader engineering applications.

2. Methods

Gas atomized AlSi7Mg alloy powder (LPW South Europe) with size of 20–63 μm was used for the experiments. The chemical composition of the powder is provided in Table S2. The PBF-LB process was performed under Ar gas in a Renishaw AM250. The process parameters used to produce cubes with side of 10 mm are listed in Table S3.

The specimens underwent the following heat treatments:

- As-built (AB)
- DA at 160 °C for 1 h (DA160.1), 2 h (DA160.2), 4 h (DA160.4)
- DA for 4 h at 200 °C (DA200.4), 250 °C (DA250.4), 300 °C (DA300.4)
- ST at 540 °C for 1 h followed by water quenching
- ST and aged at 160 °C for 4 h (STA160.4)

* Corresponding authors.
E-mail addresses: mauro.coduri@unipv.it (M. Coduri), riccardo.casati@polimi.it (R. Casati).

https://doi.org/10.1016/j.matlet.2025.138742
Received 9 April 2025; Received in revised form 29 April 2025; Accepted 12 May 2025
Available online 13 May 2025
0167-577X/

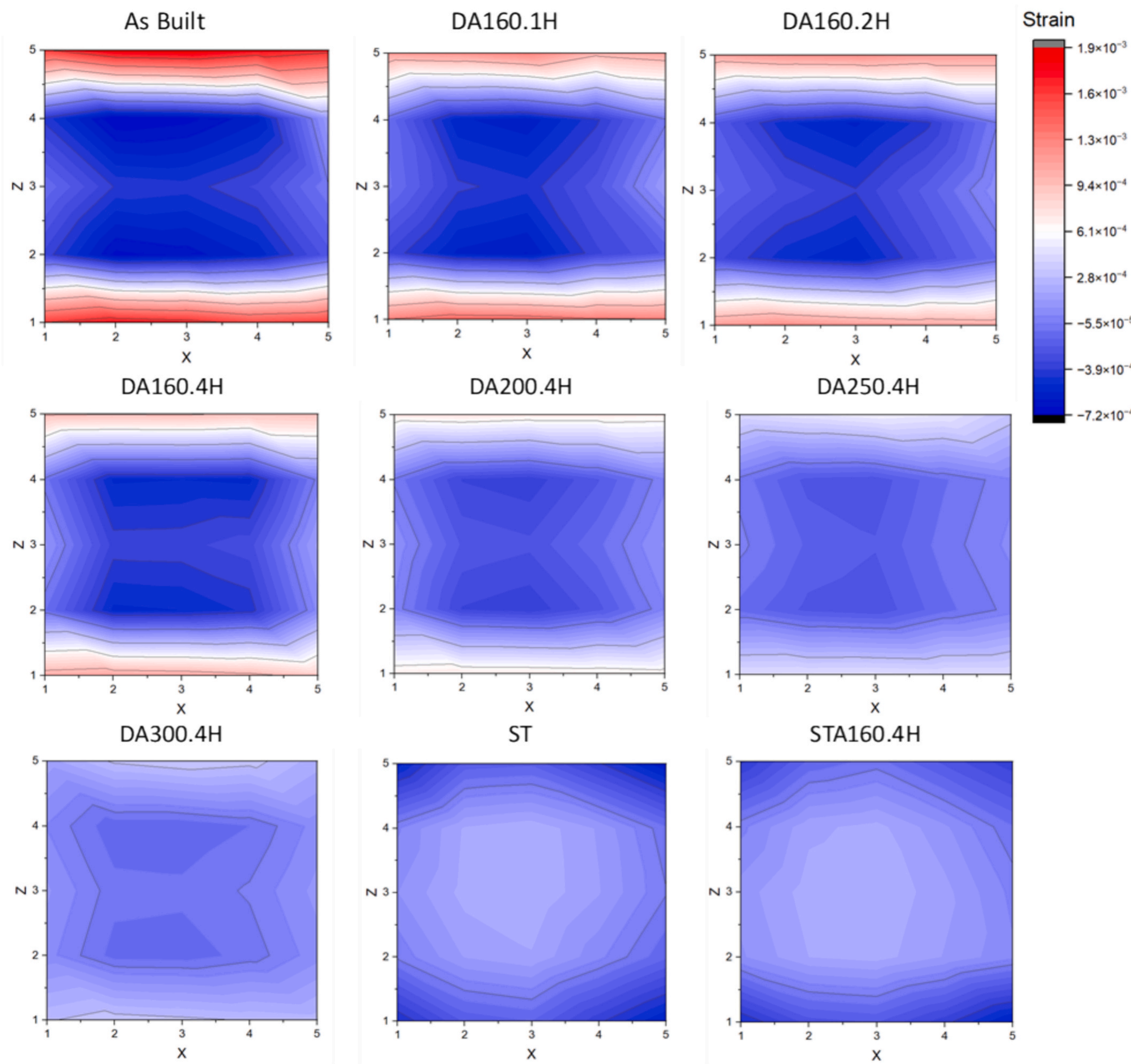

Fig. 1. Maps of longitudinal strain (i.e. strains parallel to BD) for middle layer of the investigated samples (i.e. layer in the centre of the samples and perpendicular to the BD) in Orientation 1.

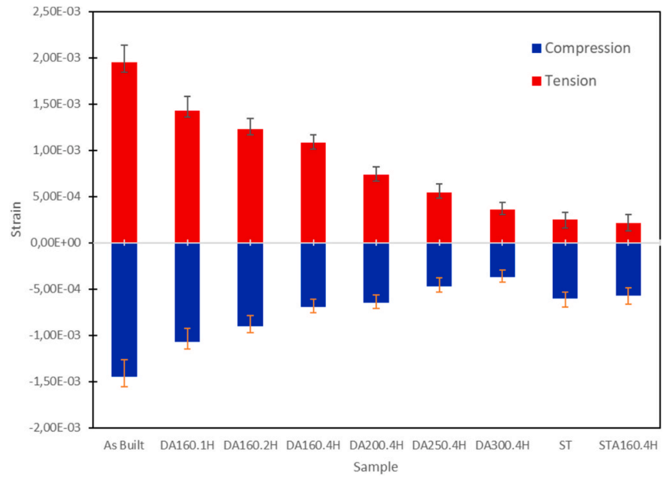

Fig. 2. Maximum longitudinal strain values measured in Orientation 1.

High resolution diffraction patterns were collected at the ID22 beamline of the ESRF, in transmission geometry at incident wavelength 0.20655 Å [6,7]. Information on the gauge volume is reported in the Supplementary Materials. The XRD signal was recorded in the 9.6°-9.8° 2θ range, corresponding to the 311 reflection of Al, selected for its experimental linear response to loading [8]. A grid of 125 points (5x5x5 in the three spatial directions) was investigated in each specimen. The *d*-spacing for each point was determined by applying Bragg's law to the peak angular position, determined by fitting with a Pseudo-Voigt function to the diffraction data. The lattice strain was determined for each point *i* using the observed *d* spacing and the reference d_0 [9,10]:

$$\varepsilon_i = \frac{d_i - d_0}{d_0}$$

where d_0 was defined as the average of all d_i values. We preferred this approach rather than extracting d_0 from a powder, as the latter would not account for the different solubility of Si and Mg after the different annealing treatments [9].

All specimens were tested with Orientation 1, i.e. with the build direction (BD) normal to the incident beam. In addition, samples AB, DA160.4, ST, and STA160.4 were also tested with Orientation 2, i.e. with BD parallel to the X-ray beam direction (Fig. S1b). IsoDEC software was used to calculate the stress from strain data (see Supplementary Material) [11,12].

3. Results & discussion

Structural, microstructural and mechanical characterization are reported elsewhere [2–4]. This work reports the residual strain and stress after selected annealing. 2D strain maps were created for each investigated layer of all the samples in Orientation 1. Fig. 1 displays the middle layer and compares samples subjected to different heat treatments. The highest value of the longitudinal strain (along BD) is found in the AB sample. Tensile strains appear close to the surface, whereas compressive strains are found in the core area. Points close to the surface were examined as near to the free surface as possible, but not exactly at the outermost layer. Thanks to the analyser crystal installed downstream the sample, no pseudo-strains arose by partial immersion. Fig. 1 shows that both treatment temperature and time effectively reduce the residual strains. Also, treatments at the typical temperature for aging of A357 (i.e. 160 °C) do not completely reduce the residual strains. Increasing the treatment temperature is indeed much more effective than increasing time. The ST specimen is characterized by very low residual strains. Subsequent artificial aging at 160 °C for 4 h further reduces such strains.

Fig. 2 displays the maximum residual strains measured in each sample along Orientation 1. The AB exhibits the highest maximum longitudinal strain. The plot allows a more precise quantification of the distinct effects of temperature and time on reducing residual strains. The T6 route (STA160.4) results in the lowest maximum residual tensile strains, while the T5 route (DA160.4) results in considerably higher residual tensile strains.

Fig. 3 presents a 3D representation of the residual stress values for each temper, along longitudinal (parallel to the BD) and transversal direction (TD). The stress data are relevant to support the design of thermal treatment aimed at finding the best trade-off between strength and residual stress. The method can potentially be extended to map the residual stresses (which significantly affect fatigue resistance [13,14]) in components featuring more complex shapes and load scenarios. This flexibility allows detailed stress mapping of components that would otherwise be difficult to assess with traditional techniques such as Barkhausen noise. The main limitation of the approach lies in the specimen absorption coefficient. For a given composition, the thicker the specimen, the higher the X-ray attenuation, the lower the signal intensity and the higher the measurement error. At 50 keV photon energy, a fully dense piece of Al 30 mm thick still allows 10 % transmittance. Such signal allows determining stresses with an error below 10 MPa. Importantly, the stress values balance to zero throughout the volume, thereby confirming that our choice of d_0 was correct.

Fig. 4 shows the maximum residual stresses detected within the volume of the samples. The highest tensile residual stress values can be found along BD, with values ranging from about 120 MPa in AB condition, down to only about 10 MPa in the solution treated specimen subjected to artificial aging. While the T5 temper provides greater strength compared to T6, as shown in Table S1, it is crucial to note that sample DA160.4 also exhibits higher residual stresses. Tensile stresses, primarily concentrated near the surface, can have a significant impact on the performance and life of components, since they can promote fatigue crack nucleation and even propagation if the compressive stresses appear at large depths. Ultimately, such tensile stresses lead to premature failure [15]. This is especially critical in applications where components are subject to high-cycle fatigue, such as in the aerospace, automotive, or energy industries. Furthermore, residual stresses can exacerbate the effects of environmental factors, such as corrosion, leading to stress-corrosion cracking, and thermal fatigue. The method proposed in this work provides a valuable tool for addressing the challenge of a proper material and component design by enabling the mapping of residual stresses in components. This technique is particularly beneficial for optimizing the process parameters and post-processing treatments of AM components, where residual stresses are often pronounced due to the layer-by-layer deposition process. By providing detailed stress maps, this approach can enable more accurate

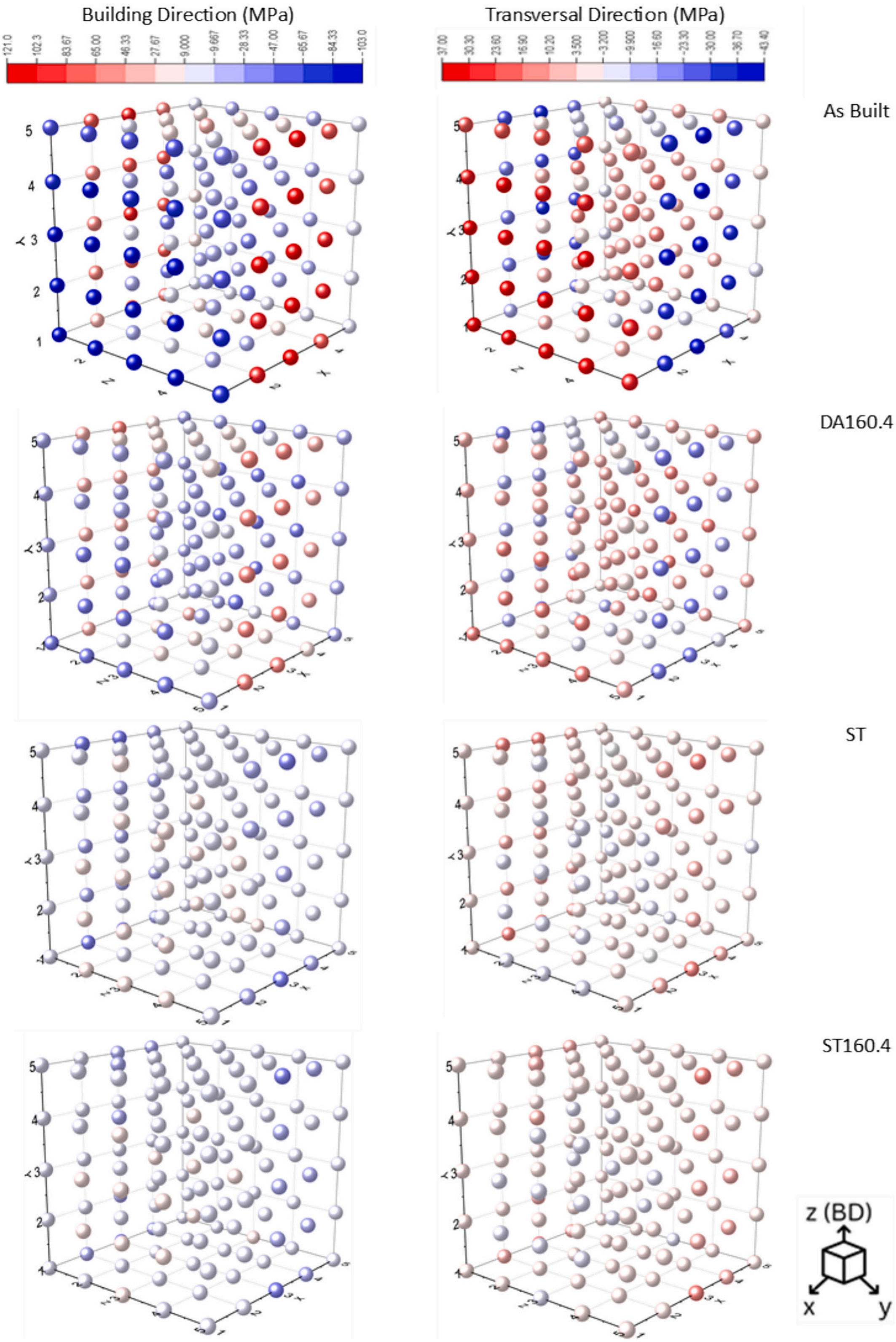

Fig. 3. 3D stress maps in longitudinal (parallel to BD) and transversal directions for as built, DA160.4, ST and STA160.4 conditions.

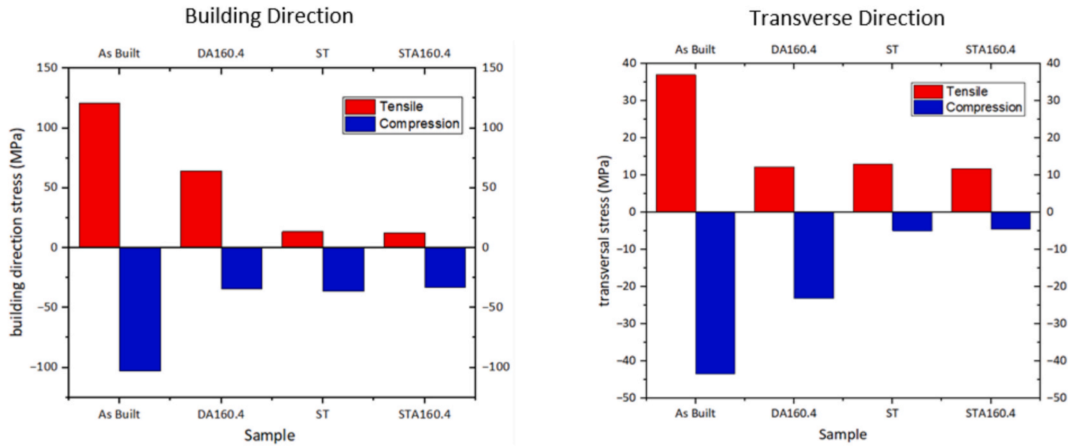

Fig. 4. Maximum stress values measured in BD and TD.

predictions of how a component will perform over time under varying load conditions, allowing better design decisions and more efficient post-processing treatments.

CRediT authorship contribution statement

A. Rahimi: Writing – original draft, Formal analysis, Data curation. **M. Coduri:** Writing – review & editing, Supervision, Formal analysis, Data curation, Conceptualization. **A. Fitch:** Writing – review & editing, Supervision, Methodology. **M. Vedani:** Writing – review & editing, Supervision, Methodology, Formal analysis. **J. Schröder:** Writing – review & editing, Methodology, Formal analysis, Data curation. **G. Bruno:** Writing – review & editing, Supervision, Methodology, Formal analysis. **R. Casati:** Writing – review & editing, Supervision, Resources, Project administration, Methodology, Investigation, Funding acquisition, Formal analysis, Conceptualization.

Declaration of competing interest

The authors declare that they have no known competing financial interests or personal relationships that could have appeared to influence the work reported in this paper.

Acknowledgements

We acknowledge the ESRF for beam time (experiment MA-5196). MC acknowledges support from the MUR and the University of Pavia through the program "Dipartimenti di Eccellenza 2023–2027".

Appendix A. Supplementary data

Supplementary data to this article can be found online at https://doi.org/10.1016/j.matlet.2025.138742.

Data availability

Data will be made available on request.

References

[1] H. Yang, et al., Defects control of aluminum alloys and their composites fabricated via laser powder bed fusion: A review, J. Mater. Process. Technol. 319 (2023) 118064.
[2] R. Casati, M. Vedani, Aging response of an A357 Al alloy processed by selective laser melting, Adv. Eng. Mater. 21 (4) (2019) 1800406.
[3] R. Casati, M. Coduri, S. Checchia, M. Vedani, Mater. Charact. 172 (2021) 110881.
[4] Casati, R.; Nasab, M. H.; Tirelli, V.; Vedani, M. Effect of Different Heat Treatment Routes on Microstructure and Mechanical Properties of AlSi7Mg, AlSi10Mg and Al-Mg-Zr-Sc Alloys Produced by Selective Laser Melting; EURO PM2018 proceedings.
[5] P. Pant, Residual Stress Distributions in Additively Manufactured Parts: Effect of Build Orientation, Thesis, Linkoping University, 2020.
[6] A. Fitch, et al., ID22 – the high-resolution powder-diffraction beamline at ESRF, J Synchrotron Rad 30 (5) (2023) 1003–1012.
[7] C. Dejoie, et al., J. Appl. Cryst. 51 (6) (2018) 1721–1733.
[8] B. Clausen, T. Lorentzen, T. Leffers, Self-consistent modelling of the plastic deformation of f.c.c. polycrystals and its implications for diffraction measurements of internal stresses, Acta Mater. 46 (9) (1998) 3087–3098.
[9] T. Fritsch, et al., On the determination of residual stresses in additively manufactured lattice structures, J. Appl. Cryst. 54 (1) (2021) 228–236.
[10] J. Schröder, et al., Texture-based residual stress analysis of laser powder bed fused inconel 718 parts, J. Appl. Cryst. 56 (4) (2023) 1076–1090.
[11] T. Gnäupel-Herold, A.A. Creuziger, M. Iadicola, A model for calculating diffraction elastic constants, J. Appl. Cryst. 45 (2) (2012) 197–206.
[12] T. Gnäupel-Herold, ISODEC: software for calculating diffraction elastic constants, J. Appl. Cryst. 45 (2012).
[13] M.N. James, et al., Synchrotron diffraction investigation of the distribution and influence of residual stresses in fatigue, Fatigue Fract. Eng. Mater. Struct. 27 (7) (2004) 609–622.
[14] K. Amjad, D. Asquith, E.A. Patterson, C.M. Sebastian, W.-C.-R. Wang, Soc. Open Sci. 4 (11) (2017) 171100.
[15] I. Roveda, et al., Influence of post-process heat treatments on the fatigue crack propagation behaviour of a PBF-LB/M AlSi10Mg alloy, Int. J. Fatigue 175 (2023) 107808.